PHYSICAL REVIEW B **95**, 144414 (2017)

Single-ion properties of the $S_{\text{eff}} = \frac{1}{2}$ XY antiferromagnetic pyrochlores $NaA'Co_2F_7$ ($A' = Ca^{2+}, Sr^{2+}$)

K. A. Ross,[1,2,*] J. M. Brown,[1] R. J. Cava,[3] J. W. Krizan,[3] S. E. Nagler,[4] J. A. Rodriguez-Rivera,[5,6] and M. B. Stone[4]

[1]*Colorado State University, Fort Collins, Colorado 80523, USA*

[2]*Quantum Materials Program, Canadian Institute for Advanced Research, Toronto, Ontario M5G 1Z8, Canada*

[3]*Princeton University, Princeton, New Jersey 08544, USA*

[4]*Quantum Condensed Matter Division, Oak Ridge National Laboratory, Oak Ridge, Tennessee 37831, USA*

[5]*NIST Center for Neutron Research, National Institute of Standards and Technology, Gaithersburg, Maryland 20899, USA*

[6]*Materials Science and Engineering, University of Maryland, College Park, Maryland 20742, USA*

(Received 17 January 2017; published 13 April 2017)

The antiferromagnetic pyrochlore material $NaCaCo_2F_7$ is a thermal spin liquid over a broad temperature range (≈140 K down to $T_F = 2.4$ K), in which magnetic correlations between Co^{2+} dipole moments explore a continuous manifold of antiferromagnetic XY states [K. A. Ross *et al.*, Phys. Rev. B **93**, 014433 (2016)]. The thermal spin liquid is interrupted by spin freezing at a temperature that is ∼2% of the mean-field interaction strength, leading to short-range static XY clusters with distinctive relaxation dynamics. Here we report the low-energy inelastic neutron scattering response from the related compound $NaSrCo_2F_7$, confirming that it hosts the same static and dynamic spin correlations as $NaCaCo_2F_7$. We then present the single-ion levels of Co^{2+} in these materials as measured by inelastic neutron scattering. An intermediate spin-orbit coupling model applied to an ensemble of trigonally distorted octahedral crystal fields accounts for the observed transitions. The single-ion ground state of Co^{2+} is a Kramers doublet with a strongly XY-like g tensor ($g_{xy}/g_z \sim 3$). The local disorder inherent from the mixed pyrochlore A sites (Na^+/Ca^{2+} and Na^+/Sr^{2+}) is evident in these measurements as exaggerated broadening of some of the levels. A simple model that reproduces the salient features of the single-ion spectrum produces approximately 8.4% and 4.1% variation in the z and xy components of the g tensor, respectively. This study confirms that an $S_{\text{eff}} = \frac{1}{2}$ model with XY antiferromagnetic exchange and weak exchange disorder serves as a basic starting point in understanding the low-temperature magnetic behavior of these strongly frustrated magnets.

DOI: 10.1103/PhysRevB.95.144414

I. INTRODUCTION

Magnetism on the pyrochlore lattice is a rich field of study that encompasses many unusual magnetic phenomena such as spin ice, spin liquids, and order by disorder (OBD) [1]. Experimental access to these phenomena has been granted mainly by rare-earth oxide pyrochlore materials. These have the general chemical formula $A_2B_2O_7$, with A a magnetic trivalent rare-earth cation and B a nonmagnetic tetravalent cation such as Ti, Sn, Zr, Ge, or Pt [1–4]. Both the A and B sites independently form a pyrochlore-type sublattice, a highly frustrated three-dimensional network composed of corner-sharing tetrahedra [Fig. 1(a)]. The anisotropic nature of the rare-earth magnetic moments, arising due to strong spin-orbit coupling (SOC) combined with crystal electric field (CEF) effects, has offered fascinating variations of magnetic behavior. For instance, local Ising anisotropy is required for generating spin ice and its emergent magnetic monopoles in $Ho_2Ti_2O_7$ and $Dy_2Ti_2O_7$ [5], while XY anisotropy can lead to OBD [6–8], as suggested for the pyrochlore material $Er_2Ti_2O_7$ [9–14]. However, the $4f$ electrons which are responsible for this magnetism have weak interaction strengths on the order of 1 K, requiring experiments to be done at millikelvin temperatures in order to access their magnetic correlations. This can limit the exploration of the lowest temperature states in these frustrated systems. Furthermore, the ground states selected by these interactions can be quite sensitive to small amounts of chemical disorder, as has been observed in $Yb_2Ti_2O_7$ [15,16] and $Tb_2Ti_2O_7$ [17].

The recently discovered $3d$ transition metal pyrochlore fluoride $NaCaCo_2F_7$ (NCCF) has previously been suggested as a strongly interacting version of the antiferromagnetic (AFM) XY pyrochlore model [18], potentially allowing for a detailed investigation of this model and its variations at lower effective temperatures. The XY anisotropy of effective spin-$\frac{1}{2}$ ($S_{\text{eff}} = \frac{1}{2}$) magnetic moments in NCCF and the related compound $NaSrCo_2F_7$ (NSCF) are confirmed here through the modeling of Co^{2+} single-ion levels by fitting to inelastic neutron scattering measurements. Furthermore, both materials are shown to have nearly identical spin correlations in their spin-frozen states, consisting of short-range ordered XY clusters and associated dynamics, despite differences in the strength of chemical disorder.

NCCF and NSCF belong to a family of $3d$ transition metal fluoride pyrochlores [19–22]. The chemical formula and structure are similar to the rare-earth oxide pyrochlores, taking the form $A_2B_2F_7$, where A is a split site of Na^+/A' ($A' = Ca^{2+}$, Sr^{2+}) and B is sixfold-coordinated Co^{2+}, Ni^{2+}, Fe^{2+}, or Mn^{2+} (Fig. 1). Unlike the previously studied fluoride-pyrochlore $CsNiCrF_6$ [23], the magnetic B site is chemically uniform, hosting just one magnetic species. The average structures of these compounds as measured by x-ray diffraction show well-ordered pyrochlores (space group $Fd\bar{3}m$), consistent with

*Corresponding author: kate.ross@colostate.edu

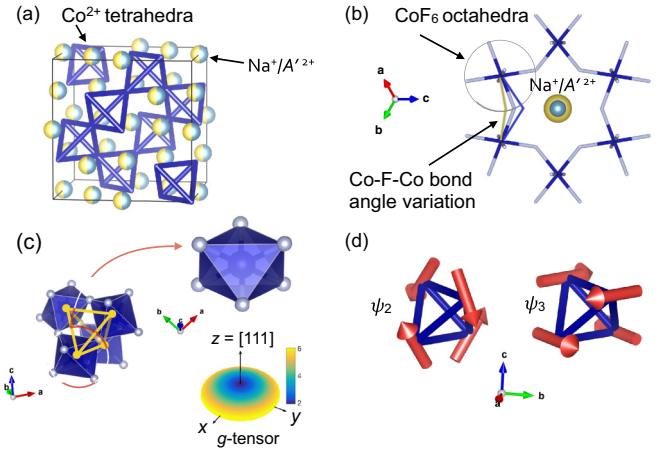

FIG. 1. (a) Depiction of the two-cation sublattices in $NaCaCo_2F_7$ and $NaSrCo_2F_7$. The $A = A'^{2+}/Na^+$ split site forms a pyrochlore sublattice (connectivity not shown here). The nearest-neighbor bonds in the $B = Co^{2+}$ pyrochlore sublattice are depicted. (b) Relationship between the A and B sites and the average atomic positions. The A-site cations reside in the open hexagons of the B-site pyrochlore structure, as viewed from the ⟨111⟩ body diagonals. The Co-F bonds are represented as rods. The yellow and blue lines illustrate potential Co-F-Co bond angle variation with A cation occupation at the central site. (c) Illustration of the average local CoF_6 octahedra, which are trigonally distorted along the local ⟨111⟩ directions that point into the center of a pyrochlore tetrahedron. The g tensor is XY-like due to this environment. (d) The two basis states forming the Γ_5 manifold, from which the static and dynamic correlations in $NaSrCo_2F_7$ and $NaCaCo_2F_7$ are selected.

random distribution of cations on the A site. Despite the materials being well ordered on average, the local structure near the B cations will be distorted away from the average trigonal D_{3d} point group due to the A-site disorder, leading to variations in exchange parameters and single-ion anisotropy [Fig. 1(b)]. In light of this, perhaps it is not surprising that all of the materials in this series eventually display spin-freezing transitions. However, the spin freezing occurs at very low *effective* temperatures; their Curie-Weiss temperatures range from $\theta_{CW} \sim -70$ [22] to -140 K [19], but the spins freeze only at 2 to 4 K. This gives large frustration indices of $f = \frac{|\theta_{CW}|}{T_F} \approx 19$ to 58, suggesting that the strength of the disorder, the presumed cause of the spin freezing, is weak compared to the overall interaction strength. An interesting comparison in this regard can be made to the B-site disordered Yb-based pyrochlore Yb_2GaSbO_7; with its $\theta_{CW} = -1.15$ K and lack of a freezing transition down to the lowest measured temperature of 20 mK, this material demonstrates similarly "ineffective" exchange disorder relative to its (much weaker) average interaction strength ($f \geqslant 58$) [24,25].

Unlike the rare-earth oxides, nearly ideal Heisenberg moments with large spins should be expected for most of the members in this new series of transition metal fluoride pyrochlores. This is due to the quenching of orbital angular momentum expected for most octahedrally coordinated 3d transition metals. This means that phenomenology such as spin ice or OBD will likely not pertain to most members of this series. The exceptions to this are the Co^{2+} compounds which we study here: NCCF and NSCF. The free ion Co^{2+} ($3d^7$) forms a ^4F ground term with $S = \frac{3}{2}$ and $L = 3$, and when placed in an octahedral coordination the CEF and SOC conspire to form an $S_{\text{eff}} = \frac{1}{2}$ single-ion ground state [26,27]. A distorted octahedral environment, such as the average environment of NCCF and NSCF, will lead to single-ion anisotropy in the $S_{\text{eff}} = \frac{1}{2}$ states [Fig. 1(c)] [27–29]. At temperatures low enough that the ground doublet states are the only relevant degrees of freedom, it is then possible to model the interactions between effective spin-$\frac{1}{2}$ operators, in which the single-ion anisotropy encoded by the g tensor is projected into the effective exchange interactions [28,30–32]. Thus, it seems that NCCF and NSCF could serve as new "high temperature" examples in which this successful method, well developed for the rare-earth oxide series, could be used [11,31,33].

The static and dynamic spin correlations in NCCF were previously measured by inelastic neutron scattering [18]. It was found that below the freezing temperature ($T_F = 2.4$ K), short-range order (SRO) of the spins develops with a correlation length of 16 Å, corresponding to XY AFM configurations from the Γ_5 irreducible representation of the tetrahedral point group. This manifold is spanned by two basis states called ψ_2 and ψ_3, shown in Fig. 1(d). In the XY AFM pyrochlore model, the $q = 0$ long-range ordered (LRO) magnetic structures based on these two states are accidentally degenerate [6–8,34], and either one can be selected by various OBD mechanisms, as has been discussed at length in the context of $Er_2Ti_2O_7$. The observed selection of the noncoplanar ψ_2 state in that material [35] has been argued to occur either via quantum and thermal fluctuations (OBD) [9–12] or from a non-OBD mechanism involving virtual excitations to higher crystal field levels [36]. *Quenched* disorder in the form of dilution [14] or exchange disorder [13] has recently been predicted to select the coplanar ψ_3 state instead, and this has been studied in yttrium-diluted $Er_2Ti_2O_7$ [37]. In NCCF, despite a clear mechanism for exchange disorder and the presence of XY AFM correlations, an LRO state is not selected.

The low-energy inelastic neutron scattering (INS) response of NCCF shows nondispersive, diffusive excitations with a distinctive intensity vs $\vec{Q}$ pattern, extending to approximately $E = 10$ meV [18], as well as a broad distribution of relaxation times in the μeV range, as probed by NMR [38]. These dynamic signatures persist above the freezing temperature up to at least $T = 14$ K (INS [18]) and 20 K (NMR [38]). These data, combined with the high Curie-Weiss temperature ($\theta_{CW} = -140$ K) relative to the freezing temperature ($T_F = 2.4$ K) giving a frustration index of $f = 58$, show that NCCF hosts an XY thermal spin liquid, i.e., a strongly correlated but disordered state dominated by entropy, over a large temperature range. Surprisingly, NCCF resists ordering or freezing to much lower effective temperatures than the canonical XY pyrochlore $Er_2Ti_2O_7$ ($f = 20$) [39], suggesting that this material could be closer to a classical phase boundary in the general anisotropic exchange model developed for the rare-earth oxides [33]. To make further progress in modeling NCCF, it is crucial to establish the relevance of the general anisotropic pseudospin-$\frac{1}{2}$ model. This relies upon the understanding of the single-ion Hamiltonian for Co^{2+} in these materials.

In this article we first present low-energy inelastic and elastic neutron scattering measurements on the compound NSCF and compare it to the previously reported measurements on NCCF, demonstrating that despite their different A' sites the two compounds share the same experimental signatures and could be treated by the same theoretical approach. We then present the observed single-ion levels for both compounds, measured by INS over the energy range of $E = 30$–1500 meV. The observed INS response as well as the dc magnetic susceptibility are well described by a disorder-averaged intermediate SOC model. This model confirms that the single-ion ground state in both materials is a well-isolated Kramers doublet, i.e., $S_{\text{eff}} = \frac{1}{2}$, and provides the average g tensors, which are observed to be strongly XY-like and have approximately 8% variation due to local disorder.

The contents of the paper are as follows: In Sec. II we give the experimental details of the INS measurements. In Sec. III we describe the single-ion model used to fit the high-energy INS data. Section IV A demonstrates the equivalence of the spin correlations in the two materials, and presents detailed low-energy INS measurements at temperatures above T_F (i.e., the thermal spin-liquid regime). Section IV B details the single-ion results and fits. The results are further discussed in Sec. V, and conclusions from this study are presented in Sec. VI.

II. EXPERIMENTAL METHOD

Single crystals of NCCF and NSCF (space group $Fd\bar{3}m$, room temperature lattice constants $a = 10.4189$ Å and 10.545 Å, respectively) were grown via the Bridgman-Stockbarger method in an optical floating zone furnace, as previously reported [19].

We studied a 3.527 g single crystal of NSCF using the MACS spectrometer at the NIST Center for Neutron Research [40]. The dynamic structure factor, $S(\vec{Q},E)$, was measured in the $[HHL]$ reciprocal lattice plane. Neutrons with a final energy $E_f = 3.7$ meV were selected, and postsample BeO filters were used to remove higher harmonic contamination and reject neutrons for which $E_f > 3.7$ meV. For elastic scattering, a Be filter preceded the sample, while for inelastic scattering no incident filters were used. The resulting energy resolution was $\delta E = 0.17$ meV at the elastic line. These data are compared to those previously published on a 0.87 g crystal of NCCF, which was also taken using the MACS spectrometer in a similar configuration [18]. The relative masses cannot be used to compare the intensities directly due to differences in crystal mounting. The NSCF and NCCF data were scaled relative to each other to match the inelastic intensities near (002) and (111) (Fig. 2). The same scaling also produced matching (220) magnetic intensities below $T = 1.7$ K.

In order to investigate the Co^{2+} single-ion levels in NCCF and NSCF, higher energy INS experiments were performed using the SEQUOIA time-of-flight chopper spectrometer at the Spallation Neutron Source, Oak Ridge National Laboratory [41]. The crystals were oriented with $[HHL]$ in the horizontal scattering plane. Data were taken at $T = 5$ K and 200 K, using incident energies of $E_i = 60$, 250, 700, and 2500 meV. This wide range of incident energies was employed to probe the large dynamic range expected for single-ion energy levels of Co^{2+}. For these energies, the T_0 chopper and Fermi chopper

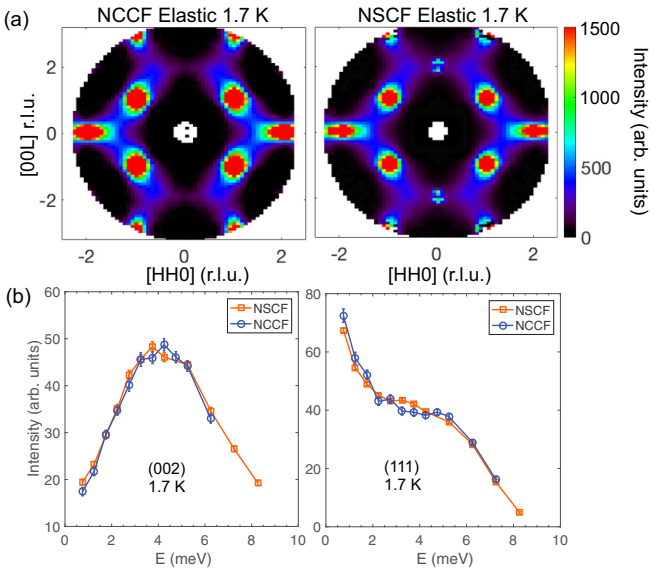

FIG. 2. Comparison of neutron scattering intensities from NSCF and NCCF. Data taken on the MACS spectrometer with energy resolution $\delta E = 0.17$ meV. (a) Magnetic elastic scattering in $NaCaCo_2F_7$ (left) and $NaSrCo_2F_7$ (right) at $T = 1.7$ K. Intensities from symmetrically equivalent quadrants of the scattering plane were averaged. The sharp feature near (002) in NSCF is due to multiple scattering and is not representative of spin correlations. (b) Constant-$\vec{Q}$ scans near the (002) and (111) positions. Error bars represent one standard deviation.

(FC1 or FC2) speeds were set to the following values: for $E_i = 60$ meV, 60 Hz (T_0) and 420 Hz (FC2); for $E_i = 250$ meV, 120 Hz (T_0) and 480 Hz (FC1); for $E_i = 700$ meV, 150 Hz (T_0) and 600 Hz (FC1); and for $E_i = 2500$ meV, 180 Hz (T_0) and 600 Hz (FC1). The elastic energy resolutions in these configurations were $\delta E = 1.92, 12.71, 44.96$, and 276.44 meV, respectively. Note that δE decreases as the neutron energy transfer increases for each E_i, and the full energy-dependent resolution for SEQUOIA [41] was employed in our fits.

III. SINGLE-ION CALCULATIONS FOR Co^{2+}

In this section we present a method for calculating the single-ion levels in Co^{2+} within an intermediate spin-orbit coupling scheme, as well as the resulting INS response and dc magnetic susceptibility. This method was used to fit the data presented in Sec. IV B. The method is similar to that used for the rare-earth-based magnets [42,43], and results in similar phenomenology. The single-ion levels for Co^{2+} in a trigonally distorted octahedron are Kramers doublets with anisotropic moments described by a g tensor.

A. Intermediate spin-orbit coupling Hamiltonian

The single-ion Hamiltonian is approximated by two contributions,

$$H_{\text{ion}} = H_{\text{CEF}}(\vec{L}) + H_{\text{SOC}}(\vec{L},\vec{S}), \tag{1}$$

where $H_{\text{CEF}}(\vec{L})$ is the crystal electric field (CEF) Hamiltonian that acts only on the orbital angular momentum subspace, and H_{SOC} is the spin-orbit coupling (SOC) term. The CEF

Hamiltonian can be written in general as

$$H_{\mathrm{CEF}} = \sum_{l,m} B_{l,m}\hat{O}_{l,m}, \tag{2}$$

where $\hat{O}_{l,m}$ are the Stevens operator equivalents [44–46]. For transition metal ions, these operators are written in terms of the orbital angular momentum matrix operators $\hat{L}_+$, $\hat{L}_-$, and $\hat{L}_z$ (as opposed to the total angular momentum operators $\hat{J}_+$, $\hat{J}_-$, and $\hat{J}_z$ relevant for f-electron systems) [45]. For the trigonal point group symmetry relevant to the average local environments of Co^{2+} in NCCF and NSCF, $(l,m) = (2,0)$, $(4,0)$, and $(4,3)$ are the only nonzero terms [45]. The $B_{l,m}$ values can be extracted by fitting to INS data.

The spin-orbit coupling term is given by

$$H_{\mathrm{SOC}} = p\lambda(\vec{S}\cdot\vec{L}) = p\lambda(\hat{S}_x\hat{L}_x + \hat{S}_y\hat{L}_y + \hat{S}_z\hat{L}_z), \tag{3}$$

where for the free ion Co^{2+} $\lambda = -22.32$ meV [47], and p is the "orbital reduction parameter" that can be used to account for changes in effective SOC strength due to covalency [26]. The x and y spin operators are linear combinations of $\hat{S}_+$ and $\hat{S}_-$ as usual: $\hat{S}_x = \frac{1}{2}(\hat{S}_+ + \hat{S}_-)$ and $\hat{S}_y = \frac{1}{2i}(\hat{S}_+ - \hat{S}_-)$, and similarly for $\hat{L}_x$ and $\hat{L}_y$.

The full single-ion Hamiltonian [Eq. (1)] can be diagonalized within the 28×28 manifold of states formed by the $|L_z,S_z\rangle$ basis of the $S = \frac{3}{2}$ and $L = 3$ free ion term (^4F) for Co^{2+}. A trigonally distorted octahedral coordination, as found in NCCF and NSCF, produces 14 Kramers doublets. The presence of a doublet ground state permits the description of the magnetic moments as pseudospin-$\frac{1}{2}$ ($S_{\mathrm{eff}} = \frac{1}{2}$) at sufficiently low temperatures. This doublet can be described as an anisotropic magnetic moment with strength given by the g tensor [27]. In the trigonal symmetry appropriate to NCCF and NSCF, the g tensor has two independent components, g_z and g_{xy}, which refer, respectively, to the local [111] direction pointing into the center of the tetrahedron, and the plane perpendicular to that [Fig. 1(c)]. The g-tensor components are given by the matrix elements of the magnetic moment operator in the subspace of the two ground state wave vectors ($|\nu_1\rangle$ and $|\nu_2\rangle$),

$$g_{xy} = -2\langle\nu_1|(\hat{L}_x + 2\hat{S}_x)|\nu_2\rangle$$

and

$$g_z = 2\langle\nu_2|(\hat{L}_z + 2\hat{S}_z)|\nu_2\rangle.$$

The resulting saturated magnetic moment sizes in the principal directions are $\mu_z = \frac{g_z}{2}\mu_B$ and $\mu_{xy} = \frac{g_{xy}}{2}\mu_B$.

B. Comparison to inelastic neutron scattering

The dynamic structure factor, $S(\vec{Q},E)$, is related to the observed intensity of inelastic neutron scattering via $I(\vec{Q},E) = \frac{k_f}{k_i}f(|Q|)^2S(\vec{Q},E)$, where k_i and k_f are the initial and final wave numbers of neutrons scattered with energy transfer $E = \frac{\hbar}{2m}(k_i^2 - k_f^2)$, and $f(|Q|)$ is the magnetic form factor [48]. The single-ion dynamic structure factor at constant $|Q|$ associated with Eqs. (1) to (3) can be calculated as follows [49]:

$$S(E) = C\sum_{n,n',\alpha}\frac{e^{-\beta E_n}}{Z}\frac{\Gamma_{\langle n,n'\rangle}|\langle\nu_n|\hat{L}_\alpha + 2\hat{S}_\alpha|\nu_{n'}\rangle|^2}{([E_{n'} - E_n] - E)^2 + \Gamma^2_{\langle n,n'\rangle}}, \tag{4}$$

where $\alpha = x,y,z$, while n and n' label eigenstates of Eq. (1). C is a scale factor applied to match the measured intensity of constant-$|Q|$ data [note that at constant $|Q|$ the form factor $f(|Q|)^2$ can be absorbed into C]. The partition function is $Z = \sum_n \exp(-\beta E_n)$ with $\beta = 1/k_BT$. $|\nu_n\rangle$ is the wave vector from the single-ion calculation corresponding to energy eigenvalue E_n. A Lorentzian half width at half maximum (HWHM), $\Gamma_{\langle n,n'\rangle}$, accounts for line broadening due to instrumental resolution, finite excitation lifetimes, or averaged dispersion of the transitions between state n and n'. To fit the data presented in Sec. IV B, we set $\Gamma_{\langle n,n'\rangle}$ to the energy-transfer-dependent instrument resolution for all transitions except those involving the ground doublet, $n = 1,2$, to the first excited doublet $n' = 3,4$. In that case, $\Gamma_{\langle n,n'\rangle} = 13.5$ meV accounts for the increased width due to the finite dispersion of the first excited level (Fig. 4). An elastic peak with a full width at half maximum (FWHM) fixed at the instrumental resolution was also added to account for all sources of nuclear elastic scattering, both coherent and incoherent.

To account for disorder in the local environment of Co^{2+} brought about by the randomly mixed A site in the crystal structures of NCCF and NSCF, the average $S(E)$ can be calculated over an ensemble of ions with slightly varying $B_{l,m}$ parameters in Eq. (2). If the local site symmetry remains trigonal, as expected based on results of vibrational spectroscopy from the related compound $NaCaMg_2F_7$ [50], there remain only three parameters that enter into H_{CEF}. For simplicity we chose a linear distribution of the $B_{4,0}$ parameter, allowing the width of the distribution ($\Delta B_{4,0}$) to be fitted. The reasoning for this choice is described in Sec. V.

C. Magnetic susceptibility

The eigenvectors and eigenvalues of Eq. (1) also permit the calculation of the (powder averaged) single-ion magnetic susceptibility as a function of temperature [49,51],

$$\chi_{\mathrm{ion}}(T) = \frac{N_A\mu_B^2}{3k_BZ}\sum_\alpha\left(\frac{\sum_n|\langle\nu_n|\hat{L}_\alpha + 2\hat{S}_\alpha|\nu_n\rangle|^2e^{-E_n/T}}{T} + \sum_n\sum_{m\neq n}|\langle\nu_m|\hat{L}_\alpha + 2\hat{S}_\alpha|\nu_n\rangle|^2\frac{e^{-E_n/T} - e^{-E_m/T}}{E_m - E_n}\right). \tag{5}$$

This expression includes the van Vleck susceptibility, but excludes the diamagnetic susceptibility χ_{dia}, and does not account for the mean-field interaction between magnetic moments. To compare to the measured dc susceptibility, the following mean-field approximation can be used [30],

$$\chi_{\mathrm{MF}} = \chi_{\mathrm{dia}} + \frac{\chi_{\mathrm{ion}}}{1 + \lambda_W\chi_{\mathrm{ion}}}. \tag{6}$$

Here, λ_W is the Weiss molecular field constant, which accounts for the mean exchange interactions. With this sign convention, a positive value of λ_W indicates AFM interactions.

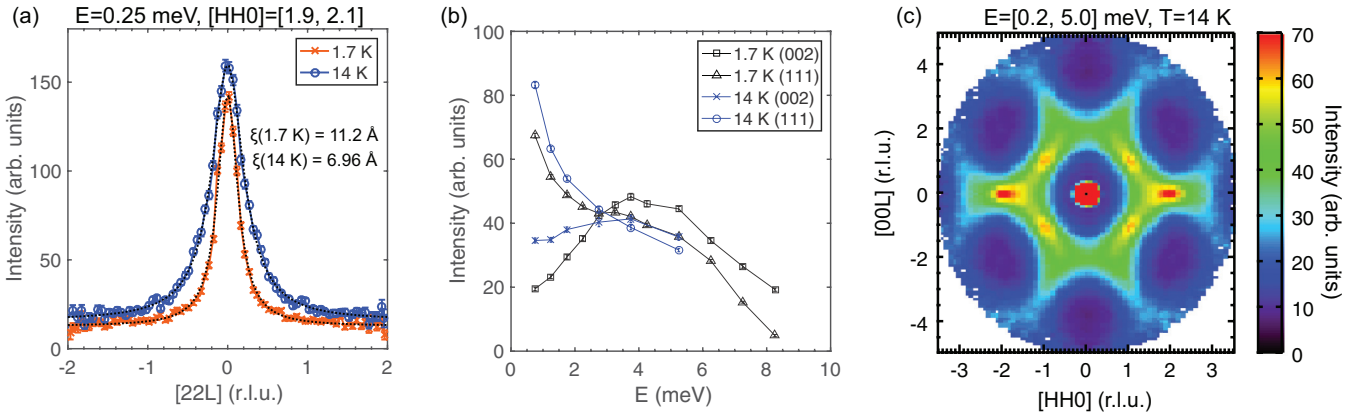

FIG. 3. Temperature dependence of inelastic scattering in NSCF. (a) Constant-energy cuts at 0.25 meV along [22L] reveal how the correlation length of the low-energy dynamics changes with increasing temperature. The dynamic correlation length along this direction decreases from 11.2 Å to 6.96 Å upon heating (dotted lines are fitted Lorentzians). (b) Constant-Q cuts near the (002) and (111) Bragg positions at $T = 14$ K and 1.7 K. (c) Diffuse inelastic scattering in NSCF above the freezing temperature, at $T = 14$ K (data folded and symmetrized, integrated from $E = 0.2$ to 5.0 meV). Error bars represent one standard deviation.

IV. RESULTS

A. Low-energy dynamic structure factor in $NaSrCo_2F_7$

The low-temperature ($T = 1.7$ K) and low-energy ($E < 5$ meV) magnetic neutron scattering response from NSCF is compared to that from NCCF in Fig. 2. The NCCF data were previously published in Ref. [18]. For the elastic scattering presented for both materials, the equivalent high-temperature ($T = 14$ K $> T_F$) elastic maps were subtracted in order to isolate the magnetic scattering. For the inelastic scattering, an empty can subtraction was performed. The neutron scattering intensity of NCCF has been scaled such that the (220) magnetic elastic peak intensity matches NSCF, which also produces equivalent intensities for the inelastic scattering. The neutron scattering patterns are nearly identical over the whole energy range, indicating that the static and dynamic spin correlations are equivalent in both compounds. An interpretation of this scattering in terms of static and dynamic XY correlations has been presented in Ref. [18]; this interpretation is expected to qualitatively apply to both materials. The sharp features near the (002) and (00$\bar{2}$) positions in NSCF seen in Fig. 2(a) appear in the elastic channel using several choices of incident energies, but can be made to vanish for other choices, signifying that their origin is multiple scattering. Such (002) scattering has been observed before in rare-earth titanates and was previously thought to be caused by symmetry lowering, but has recently been identified as multiple scattering in those materials as well [52].

The data shown in Fig. 2 were collected below the freezing temperatures of NCCF and NSCF (2.4 K and 3.0 K, respectively). Above the freezing transition, it was shown previously in NCCF that the elastic magnetic scattering vanishes, while inelastic magnetic scattering at $E = 0.5$ meV persists to at least $T = 14$ K and retains the same distinctive pattern in reciprocal space [18]. In NSCF we have confirmed the persistence of this inelastic scattering above T_F at $T = 14$ K. The inelastic scattering at $E = 0.25$ meV is broader at 14 K compared to 1.7 K, implying shorter ranged dynamic correlations [Fig. 3(a)]. The full energy dependence of the scattering up to 5 meV is compared for the two temperatures in Fig. 3(b), which shows that the spectrum has similar features above and below T_F, but with enhanced low-energy spectral weight at $T = 14$ K. The energy-integrated scattering at $T = 14$ K in NSCF ($E = 0.2$ to 5.0 meV) over the [HHL] plane is shown in Fig. 3(c). This scattering could be compared to equal-time correlation functions, such as those calculated in Ref. [33].

B. Single-ion levels and average g tensors of $NaSrCo_2F_7$ and $NaCaCo_2F_7$

Transitions between single-ion levels of Co^{2+} were observed in NCCF and NSCF using the SEQUOIA time-of-flight neutron spectrometer. The energies of the observed transitions were found range from 28 to 908 meV, requiring the use of multiple incident energies. The first excited level measured using $E_i = 60$ meV in both NCCF and NSCF is shown in Fig. 4, at both $T = 5$ and 200 K. In both materials this level

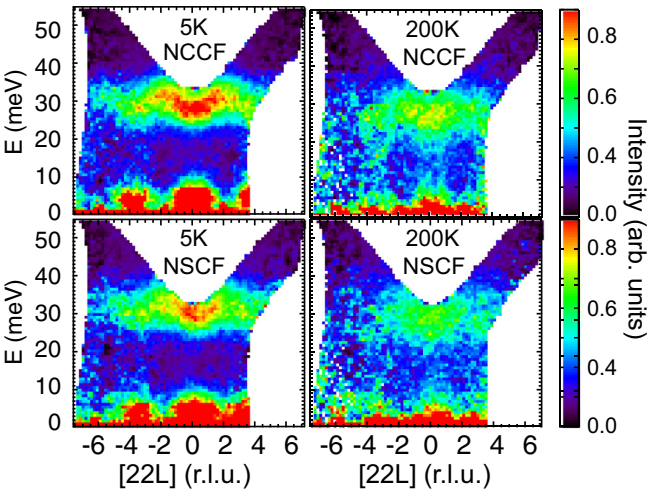

FIG. 4. The first excited single-ion levels in NCCF (top row) and NSCF (bottom row), observed by inelastic neutron scattering ($E_i = 60$ meV). Data are averaged over the following ranges in perpendicular reciprocal lattice directions (r.l.u.): [$HH0$], $H = [1.9,2.1]$, and [K-$K0$], $K = [-0.1,0.1]$.

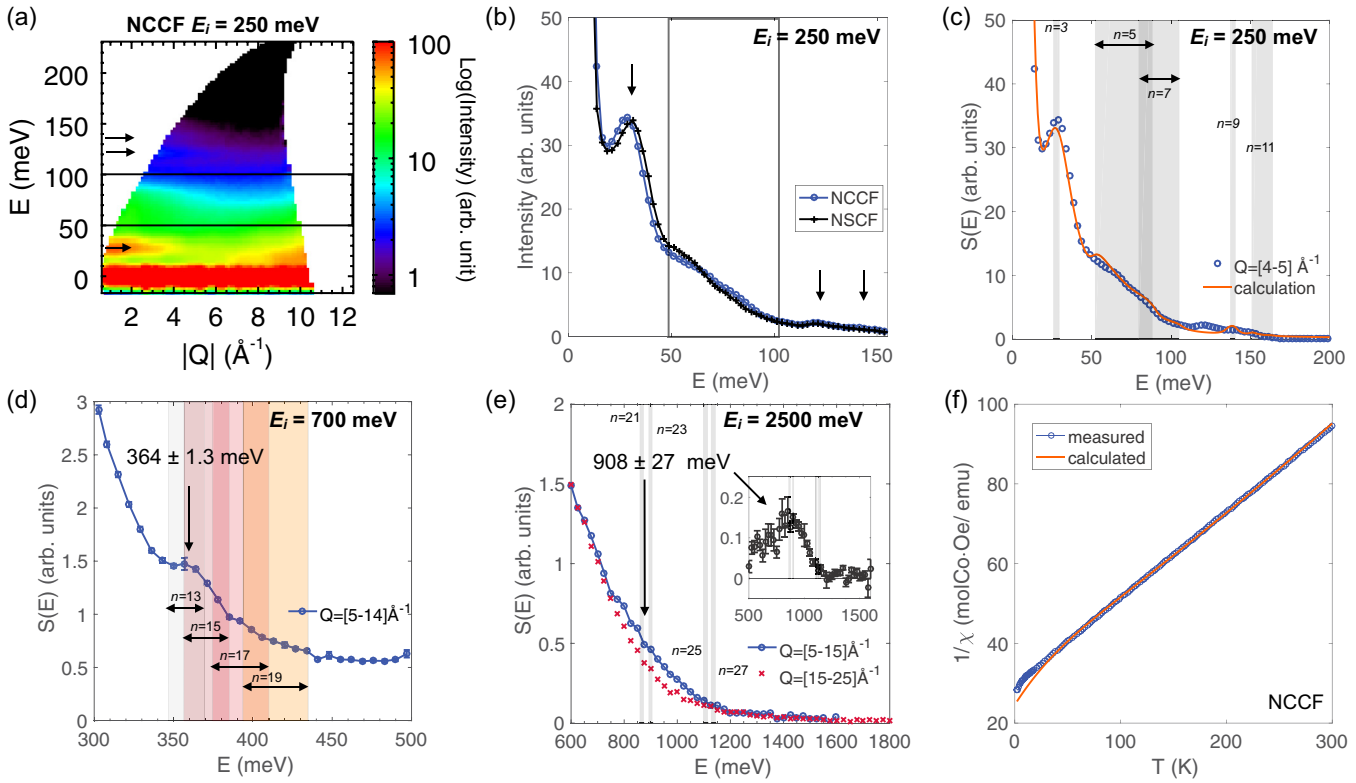

FIG. 5. Measurements and fits of single-ion levels of Co^{2+} in $NaCaCo_2F_7$. Panels (a) through (e) show the observed single-ion levels from orientationally averaged single-crystal inelastic neutron scattering measurements (SEQUOIA spectrometer), at $T = 5$ K. Shaded regions in panels (c) to (e) indicate the energy ranges spanned by the doubly degenerate eigenvalues of Eq. (1); the eigenvalues vary for different local environments, producing a range of values (see main text). The first eigenstate label, n, in the corresponding doublet is indicated for each range. (a) Energy vs $|Q|$ pseudocolor plot, with $E_i = 250$ meV. Intensity is displayed on a logarithmic scale. Arrows indicate the positions of relatively sharp magnetic modes, and the rectangle indicates a broad band of magnetic scattering. (b) Cut through data in panel (a), and equivalent data from NSCF, averaging from $|Q| = 4$–5 Å^{-1} (empty can background subtracted). (c) Fit to the NCCF data shown in panel (b). (d) $E_i = 700$ meV, averaging from $|Q| = 5$–14 Å^{-1}. (e) $E_i = 2500$ meV, cuts taken at both high and low $|Q|$. On top of a steep nonmagnetic background, additional intensity is seen for low $|Q|$ near 900 meV. The inset shows the subtraction of the high-$|Q|$ background, which gives a peak at 908 ± 27 meV. (f) Single-ion susceptibility with mean-field interactions [Eqs. (5) and (6)] compared to the measured dc susceptibility of NCCF from Ref. [19].

is located near 30 meV, persists to temperatures above $|\theta_{CW}|$ (demonstrating its single-ion origin), and displays the characteristic decreasing intensity vs $|Q|$ dependence of magnetic excitations [Fig. 5(a)]. At $T = 5$ K the first excited level displays distinct dispersion, suggesting exchange-induced mixing of the ground state and first excited level [26]. Note that the low-energy spin excitations presented in Sec. IV A are also identifiable in Fig. 4 below ∼10 meV; these are due to the magnetic correlations discussed in Ref. [18], rather than single-ion levels.

The full set of observed single-ion levels in NCCF at $T = 5$ K is shown in Fig. 5 along with results of fitting the model described in Sec. III. Some of these features are significantly broader than the energy resolution as expected, since the local variation in Co environment should produce finite energy ranges over which transitions are observed. The measured energies of the single-ion levels and corresponding energy widths are tabulated in Table I for both NCCF and NSCF [53]. All neutron scattering data in Fig. 5 have a corresponding background subtracted and are corrected for the k_f/k_i factor described in Sec. III B, thus representing the quantity $f(|Q|)^2 S(Q,E)$ in arbitrary units. The orientational average of these single-crystal data is presented in order to provide a concise overview of the excitations; no significant dispersion was detectable in any but the first excited level,

TABLE I. Measured single-ion levels in $NaCaCo_2F_7$ (NCCF) and $NaSrCo_2F_7$ (NSCF), with central peak positions and full width at half maxima (FWHM). Due to time constraints, the peak expected near 360 meV in NSCF was not measured. The quoted error on the peak centers is the standard deviation of the fitted peak center. None of the observed modes have resolution-limited widths. Instrument configurations are indicated by a: $E_i = 250$ meV, b: $E_i = 700$ meV, c: $E_i = 2500$ meV.

NCCF		NSCF	
Energy (meV)	FWHM (meV)	Energy (meV)	FWHM (meV)
28.05(2)^a	27.50(7)	29.31(2)^a	29.53(8)
∼46–101^a	broad	∼41–100^a	broad
121.9(1)^a	9.1(4)	120.7(2)^a	7.2(9)
∼139^a	broad	∼134^a	broad
364(1)^b	24(3)		
9.1(3)×10$^{2\ c}$	3.2(6)×10^2	9.0(3)×10$^{2\ c}$	3.7(6)×10^2

and this dispersion is well accounted for in the model by an increased FWHM, as discussed below. For a uniform Co^{2+} environment, 14 levels (including the ground state) are expected in total, each of them doubly degenerate according to the Kramers theorem. Note that at $T = 5$ K, a low temperature compared to the energy of the first excited level (~300 K), only transitions from the ground state to the excited states will be observable. Additionally, some of these transitions may have weak intensities, depending on the strength of the transition matrix elements between eigenstates of Eq. (1). The intensities are weighted by the square of the transition matrix elements of the magnetic moment operator, $M^2_{\langle n,n'\rangle} = \sum_\alpha |\langle \nu_n|\hat{L}_\alpha + 2\hat{S}_\alpha|\nu_{n'}\rangle|^2$, which enter into Eq. (4).

Figure 5(a) shows measurements at $E_i = 250$ meV, with the intensity presented on a logarithmic color scale. This shows several of the magnetic excitations, including the first excited level near 30 meV (as in Fig. 4), a broad band of magnetic features spanning approximately 46 to 100 meV (indicated by a rectangle), and two higher energy features near 120 and 140 meV. Note that phonon scattering is also visible below 30 meV, but its intensity increases as a function of $|Q|$, while the magnetic features show the opposite trend in intensity vs $|Q|$ due to the magnetic form factor (see also the Appendix). Intensity vs energy cuts from $Q = [4,5]$ Å^{-1} are compared for NCCF and NSCF in Fig. 5(b), showing the overall similarity between the single-ion levels in the two compounds. The first excited level is at a slightly higher energy for NSCF [29.31(2) meV] compared to NCCF [28.05(2) meV]. Two higher energy levels are shown in Figs. 5(d) and 5(e), located at 364 ± 1 meV and 908 ± 30 meV. In these high-energy ranges, multiphonon scattering creates a strong, sloping background and obscures these magnetic features. Nevertheless, their magnetic nature is confirmed by their $|Q|$ dependence. For the data shown in panel (d), the single-ion level energy was extracted using a fit that included a sloping background plus a Gaussian. For the 908 meV feature, intensities vs E for two $|Q|$ ranges were compared, as shown in panel (e). The precision of the energy determination for these higher modes is relatively poor due to decreased energy resolution of the higher incident energy instrument configurations.

Fits to these measured single-ion levels were carried out using a least-squares minimization routine. The dynamic structure factor at constant $|Q|$, i.e, $S(E)$, was calculated from the single-ion model with local trigonal disorder described in Sec. III, and was compared to the $E_i = 250$ meV data averaged from $|Q| = 4$–5 Å^{-1} [Fig. 5(c)]. The measured energies and uncertainties of the higher excited levels (364 ± 1 meV and 908 ± 30 meV) were included as constraints on the minimization, but no attempt was made to compare their relative intensities, which are difficult to accurately determine due to instrumental effects. The HWHM parameters $\Gamma_{\langle n,n'\rangle}$ in Eq. (4) were held fixed to the calculated instrumental resolution for most values of n and n', but were increased to 13.5 meV for $n = 1,2$ and $n' = 3,4$ to account for the dispersion of the first excited level. The coherent and incoherent nuclear elastic scattering was modeled by a Gaussian with FWHM fixed to the instrumental resolution ($\delta E = 12.7$ meV), and the area of that elastic signal was used as an additional fitting parameter (C_E). In total there were seven fitting parameters; the three average crystal field parameters ($B_{2,0}$, $B_{4,0}$, and $B_{4,3}$), a width of the linear distribution of $B_{4,0}$ ($\Delta B_{4,0}$), the orbital reduction parameter p, the elastic line area C_E, and an overall scale factor C. These fitted parameters and the associated average g tensors with their percent variation are listed in Table II. The energy eigenvalues for the average $B_{l,m}$, their variation over the full $\Delta B_{4,0}$ range, as well as transition matrix elements, are listed in Table III. The energy levels as a function of $B_{4,0}$ are visualized in Fig. 6. Note that due to the overall similarity between the single-ion levels of NCCF and NSCF, as well as the limited accuracy of the simple model of local disorder (as discussed in Sec. V), only one set of parameters is presented. Although this fit is not likely to be unique in the sense that the broad observed transitions and minimal modeling of disorder prevent a precise determination of the parameters, the obtained parameters adequately capture the main features of the single-ion levels in both materials and provide the key physical insights that can be gained from these data.

TABLE II. Parameters for the single-ion Hamiltonian, fitted to inelastic neutron scattering data in NCCF. The values of g_z and g_{xy} are those obtained from the mean value of the CEF parameters (i.e., when $\Delta B_{4,0} = 0$).

Parameter	Fitted value	Variation
$B_{2,0}$	25.8(5) (meV)	
$B_{4,0}$	0.455(5) (meV)	
$B_{4,3}$	14.01(7) (meV)	
$\Delta B_{4,0}$	0.127(4) (meV)	
p	1.021(4)	
g_z	1.87	8.4%
g_{xy}	6.08	4.1%

TABLE III. Calculated energy levels (in meV) from the fit shown in Fig. 5, and the corresponding energy ranges arising from the variation in a crystal field parameter ($\Delta B_{4,0}$) which was used to model the local disorder at the Co^{2+} site. The sum of the square of the transition matrix elements from the ground doublet to each excited doublet are listed, for the average CEF parameters ($M^2_{\langle n,n'\rangle} = \sum_\alpha |\langle \nu_n|\hat{L}_\alpha + 2\hat{S}_\alpha|\nu_{n'}\rangle|^2$). Note that not all of the transitions listed in this table have been observed; refer to Fig. 5 for the correspondence between the measured and calculated peak positions.

State ($\nu_{n'}$)	$E_{n'}$ for $\Delta B_{4,0} = 0$	Range of $E_{n'}$	$M^2_{\langle 1,n'\rangle} + M^2_{\langle 2,n'\rangle}$
ν_1, ν_2	0.0	0.0	19.48
ν_3, ν_4	27.7	3.5	17.06
ν_5, ν_6	69.4	36.1	3.55
ν_7, ν_8	90.0	25.4	0.37
ν_9, ν_{10}	135.4	3.03	0.12
ν_{11}, ν_{12}	154.3	13.0	0.04
ν_{13}, ν_{14}	355.6	22.6	0.51
ν_{15}, ν_{16}	367.6	28.6	0.67
ν_{17}, ν_{18}	389.3	35.6	0.83
ν_{19}, ν_{20}	411.1	41.1	0.17
ν_{21}, ν_{22}	863.9	13.5	0.11
ν_{23}, ν_{24}	896.7	12.2	0.71
ν_{25}, ν_{26}	1103.9	16.5	0.02
ν_{27}, ν_{28}	1133.3	15.8	0.01

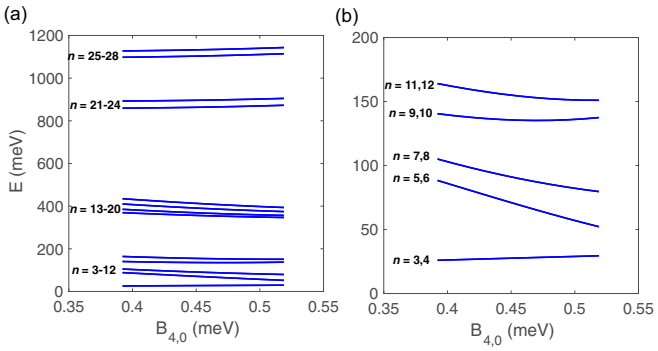

FIG. 6. (a) Energy eigenvalues as a function of $B_{4,0}$. The eigenstates are labeled by n. (b) Expanded view of the low-energy part of panel (a).

Finally, the high-temperature dc magnetic susceptibility can be compared to the measured susceptibility of NCCF from Ref. [19], using the average $B_{l,m}$ parameters shown in Table II. Fitting the inverse susceptibility from $T = 100$–300 K using Eqs. (5) and (6), the two parameters $\chi_{\rm dia} = -3.1(1)\times10^{-4}$ emu/mol and $\lambda_W = 23.99(5)$ mol/emu were determined, and excellent agreement is found with the high-temperature data [Fig. 5(f)]. This agreement further confirms the validity of the single-ion scheme determined from the neutron scattering results.

V. DISCUSSION

1. Single-ion model

The single-ion fits suggest that the reduction of spin-orbit coupling (quantified by p) is not significant, since it refines to 1.021(4), which is nearly 1.0. This is in contrast to $KCoF_3$, for which $p = 0.93$ [26], indicating orbital moment reduction due to covalency. Thus, naively, NCCF and NSCF seem to have strongly ionic bonds.

The model used to fit the single-ion levels, presented in Sec. III, accounts for the local disorder in a minimal way. The local symmetry at the Co^{2+} site is assumed to remain trigonal, based on vibrational spectroscopy of the nonmagnetic structural analog $NaCaMg_2F_7$ from Ref. [50]. In that study it was found that the number and selection rules of vibrational modes was inconsistent with the full $Fd\bar{3}m$ symmetry of the average structure, but could be accounted for using the $F4\bar{3}m$ subgroup. Using the online software package ISODISTORT [54], and assuming atomic displacements consistent with this symmetry lowering, we find that the point group of the Co site remains trigonal, but is reduced from D_{3d} to C_{3v} (note that on average, these local distortions would cancel out and produce the $Fd\bar{3}m$ space group that is observed for the average structure). This implies that only three CEF parameters are required, but that there may be some variation in their values from site to site, as the Co-F bond angles and distances (and therefore the CEF) are modified by the local disorder. In the absence of a more realistic model for the distribution of local disorder, we initially allowed a linear variation in each of the crystal field parameters in Eq. (2) and averaged the calculated $S(E)$ for each set of parameters. We found that only a variation in $B_{4,0}$ (which we call $\Delta B_{4,0}$) was necessary to reproduce the observed widths and positions of the peaks observed via INS (Fig. 5). Specifically, the energies of the ν_5, ν_6 and ν_7, ν_8 doublets are more widely distributed compared to the other levels, consistent with the broad band of magnetic intensity observed between ∼40 and 100 meV in INS, without creating excessive widening (beyond the measured widths) of the higher energy levels. It may be noted that this model does not perfectly account for the intensities and positions of all features, particularly near the modes near 121 meV. This is not unexpected, as the model we are using for the disorder is simplified. The numerical values we report for the g tensor and its variation ($g_z = 1.87 \pm 8.4\%$ and $g_{xy} = 6.08 \pm 4.1\%$) can nevertheless be used as good estimates.

A more accurate model of the disorder could perhaps be developed based on additional experimental information about the local structure of these materials. To this end, a ^{23}Na NMR study of NCCF has revealed an unusual high temperature response suggesting that there are two main crystallographic environments for Na [38]. So far no model to explain this observation has been proposed. A measurement of the neutron or x-ray pair distribution function (PDF) could provide additional information.

Although there remains some uncertainty in the distribution of g-tensor values, the results of our single-ion study unequivocally indicate that NSCF and NCCF are XY pyrochlores with well-isolated Kramers doublets. This doublet nature of the low-energy degrees of freedom is consistent with estimates of the spin entropy from specific heat which reach nearly $R \ln 2$ per mole of Co [19,20], as well as with the sum rule analysis of low-energy neutron scattering intensities [18]. Our results show that interactions in these materials may be treated within a pseudospin-$\frac{1}{2}$ model with XY effective exchange. If the dominant interactions occur between nearest neighbors, this would produce a model similar to the one used to describe $Er_2Ti_2O_7$ and $Er_2Sn_2O_7$ [10,11,32]. The variation in the g tensor implies that exchange disorder is needed in the effective model.

2. Susceptibility

The dc susceptibility in both NSCF and NCCF can be well accounted for by the single-ion model used with the average $B_{l,m}$ parameters reported in Table II. The model naturally explains the high effective moments of these two materials (∼6 μ_B) as determined from Curie-Weiss fits of the inverse susceptibility over the range 100 K to 300 K [19]. Another feature of the model is a downturn in $1/\chi$ near 50 K; this experimentally observed feature was previously assumed to be due to ferromagnetic correlations, but it can now be understood as changes in the thermal population of excited single-ion levels. The fitted Weiss molecular field constant, $\lambda_W = 23.99(4)$ mol/emu, confirms that AFM interactions are dominant, in agreement with the low-energy INS results.

3. Comparison of $NaCaCo_2F_7$ and $NaSrCo_2F_7$

The neutron scattering results presented in Sec. IV indicate that the magnetic correlations and single-ion properties of NSCF and NCCF are nearly identical. NCCF and NSCF have freezing temperatures of 2.4 K and 3.0 K, respectively. The increased freezing temperature of NSCF seems likely to be related to the larger differential ionic radius on the A site: for eightfold-coordinated Na^+, $r = 1.18$ Å; for Ca^{2+},

$r = 1.12$ Å; and for Sr^{2+}, $r = 1.26$ [55]. The bigger this size difference, the more severe the local disorder is expected to be. The measured single-ion levels are very similar, with the only notable difference being the position of the first excited level, which is slightly higher in energy for NSCF compared to NCCF. However, within the accuracy of our model, there is no discernible difference in the single-ion ground state wave functions. Thus, it seems likely that both NSCF and NCCF could be treated within the same low-energy effective model, but the strength of exchange disorder should be enhanced for NSCF.

4. Co^{2+} pyrochlores

Given the promise of extending the phenomenology of anisotropic rare-earth pyrochlores to materials with higher interaction strengths, searching for other Co^{2+}-based pyrochlores seems desirable. To the best of our knowledge, only one other material has been reported with a Co^{2+} pyrochlore sublattice: the spinel $GeCo_2O_4$. This material has been discussed in terms of its $S_{\text{eff}} = \frac{1}{2}$ single-ion ground state, and some unusual details of the higher energy excitation spectrum have been modeled in terms of molecular magnetism involving neighboring tetrahedra of these $S_{\text{eff}} = \frac{1}{2}$ moments [56]. In $GeCo_2O_4$ the CoO_6 octahedra are not distorted, and the moment is therefore isotropic.

An interesting question for future exploration is whether there exists a Co^{2+}-based *spin ice* material (either quantum or classical). Such a material would have the advantage that the emergent monopole dynamics would occur at temperatures much easier to access, possibly even high enough to be useful for applications. If the U(1) quantum spin liquid phase of *quantum* spin ice could be produced in a Co^{2+} pyrochlore, its emergent photon modes would have a more accessible bandwidth compared to the rare-earth-based candidates, making them more easily identifiable with low-energy inelastic neutron scattering and thermodynamic measurements. To achieve the necessary Ising anisotropy within a Co^{2+} pyrochlore, the octahedral environment would need to be *elongated* along the ⟨111⟩ directions rather than compressed as it is for NCCF and NSCF.

VI. CONCLUSIONS

We have presented inelastic neutron scattering results on the pyrochlore materials $NaCaCo_2F_7$ and $NaSrCo_2F_7$. The low-energy response of $NaSrCo_2F_7$ (below 10 meV) confirms that it hosts the same type of spin correlations as $NaCaCo_2F_7$, which are fully dynamic above the freezing temperatures (2.4–3.0 K) but static and short-range correlated below. These correlations are well described in terms of static and dynamic antiferromagnetic XY spin clusters, as discussed in Ref. [18]. Below T_F, the XY configurations are frozen, short-range correlated versions of the ψ_2 and ψ_3 states which are known to be selected through various types of order by disorder in the XY AFM models of the pyrochlore lattice.

Our main result is the measurement and analysis of the single-ion levels of Co^{2+} in these materials. These are well modeled by an intermediate spin-orbit coupling Hamiltonian. We incorporated a distribution of crystal field parameters to account for local disorder brought about by the split nonmagnetic A site. The ground state of Co^{2+} in these environments is always a Kramers doublet with an XY g tensor. The average crystal field parameters produce $g_z = 1.87$ and $g_{xy} = 6.08$, with a variation of 8.4% and 4.1%, respectively. The single-ion ground state doublets are separated from the first excited states by ∼300 K. Thus, at low temperatures ($T < \theta_{CW} \sim 150$ K), where spin correlations develop, a low-energy effective theory built from $S = \frac{1}{2}$ operators can be used to describe these materials. Due to the XY g tensor and its variation, the effective exchange interactions are likely to be XY-like with bond (exchange) disorder. A basic model of the AFM XY pyrochlore with exchange disorder has been predicted to lead to a long-range ordered state. However, $NaCaCo_2F_7$ and $NaSrCo_2F_7$ do not seem to conform to this prediction.

In summary, our results show that these materials can be thought of as "high temperature" versions of the $S_{\text{eff}} = \frac{1}{2}$ AFM XY pyrochlore, which has been studied in relation to the rare-earth oxide series of pyrochlores. Their strong interactions allow the exploration of a wider temperature range of this model. The inherent local disorder arising from the split nonmagnetic A site is likely to produce exchange disorder, in part through the local variations of the g tensor that we have estimated here. The role of this exchange disorder in a model appropriate to these materials requires more investigation, as the ground states appear to be contrary to the prediction that *quenched* order by disorder selects long-range order. Finally, $NaCaCo_2F_7$ and $NaSrCo_2F_7$ are more frustrated ($f \sim 50$) versions of the AFM XY pyrochlore than the canonical example, $Er_2Ti_2O_7$ ($f = 20$). This may indicate that they are closer to a phase boundary in the general anisotropic exchange model developed for the pyrochlore lattice; this proximity would make the materials more sensitive to quantum fluctuations, and may even put them in proximity to a quantum disordered phase.

ACKNOWLEDGMENTS

The authors gratefully acknowledge discussions with K. Kimura, the use of software adapted from work by G. Hester and J. O'Brien, and the encouragement of C. L. Broholm. The neutron scattering data were reduced using the Mantid [57] and DAVE [58] software packages. The crystal growth activities

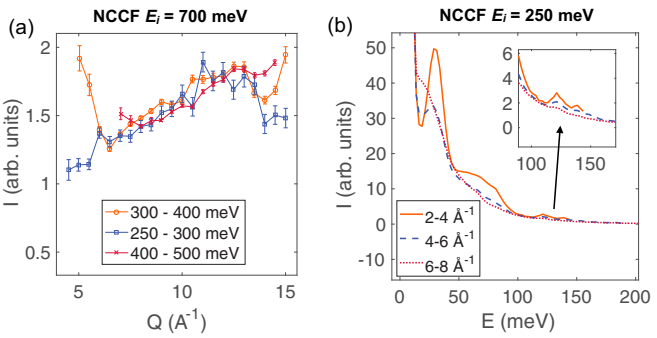

FIG. 7. (a) Q dependence of intensity for energy ranges spanning the identified single-ion mode at ∼360 meV (300 to 400 meV), just above the single-ion mode (400 to 500 meV, intensity shifted up for comparison), and just below the single-ion mode (250–300 meV, intensity shifted down for comparison). (b) Energy dependence of neutron scattering intensity in different Q ranges for $E_i = 250$ meV.

at Princeton were supported by the US Department of Energy, Office of Basic Energy Sciences, Division of Material Sciences and Engineering, under Grant No. DE-FG02-08ER46544. This work utilized neutron scattering facilities supported in part by the National Science Foundation under Agreement No. DMR-1508249. A portion of this research used resources at the Spallation Neutron Source, a DOE Office of Science User Facility operated by the Oak Ridge National Laboratory.

APPENDIX: Q DEPENDENCE OF MODES OBSERVED WITH $E_i = 700$ meV AND 250 meV

The inelastic modes shown in Figs. 5(a)–5(d) can be identified as being magnetic in origin due to the $|Q|$ dependence of their intensities. The intensity of magnetic features (such as single-ion levels) should decrease with increasing $|Q|$ due to the magnetic form factor [59]. Meanwhile the intensity of features arising from phonons (whether single- or multiphonon processes) should show the opposite trend. For the mode identified near 360 meV in NCCF (using $E_i = 700$ meV), the $|Q|$ dependence of intensity reveals a combination of both magnetic and multiphonon contributions. This is demonstrated in Fig. 7(a), which compares intensity near 360 meV to that in energy ranges just above and just below the observed mode. This demonstrates that the peak observed near 360 meV is magnetic in origin. The intensity of the features observed using $E_i = 250$ meV are also shown for three different Q ranges in panel (b), demonstrating their magnetic nature.

[1] J. S. Gardner, M. J. P. Gingras, and J. E. Greedan, Rev. Mod. Phys. **82**, 53 (2010).
[2] R. D. Shannon and A. W. Sleight, Inorg. Chem. **7**, 1649 (1968).
[3] Z. L. Dun, X. Li, R. S. Freitas, E. Arrighi, C. R. D. Cruz, M. Lee, E. S. Choi, H. B. Cao, H. J. Silverstein, C. R. Wiebe *et al.*, Phys. Rev. B **92**, 140407 (2015).
[4] Y. Q. Cai, Q. Cui, X. Li, Z. Dun, J. Ma, C. dela Cruz, Y. Jiao, J. Liao, P. Sun, Y. Q. Li *et al.*, Phys. Rev. B **93**, 014443 (2016).
[5] C. Castelnovo, R. Moessner, and S. L. Sondhi, Annu. Rev. Condens. Matter Phys. **3**, 35 (2012).
[6] S. T. Bramwell, M. J. P. Gingras, and J. N. Reimers, J. Appl. Phys. **75**, 5523 (1994).
[7] A. W. C. Wong, Z. Hao, and M. J. P. Gingras, Phys. Rev. B **88**, 144402 (2013).
[8] P. A. McClarty, P. Stasiak, and M. J. P. Gingras, Phys. Rev. B **89**, 024425 (2014).
[9] J. D. M. Champion, M. J. Harris, P. C. W. Holdsworth, A. S. Wills, G. Balakrishnan, S. T. Bramwell, E. Čižmár, T. Fennell, J. S. Gardner, J. Lago *et al.*, Phys. Rev. B **68**, 020401 (2003).
[10] M. E. Zhitomirsky, M. V. Gvozdikova, P. C. W. Holdsworth, and R. Moessner, Phys. Rev. Lett. **109**, 077204 (2012).
[11] L. Savary, K. A. Ross, B. D. Gaulin, J. P. C. Ruff, and L. Balents, Phys. Rev. Lett. **109**, 167201 (2012).
[12] J. Oitmaa, R. R. P. Singh, B. Javanparast, A. G. R. Day, B. V. Bagheri, and M. J. P. Gingras, Phys. Rev. B **88**, 220404 (2013).
[13] V. S. Maryasin and M. E. Zhitomirsky, Phys. Rev. B **90**, 094412 (2014).
[14] A. Andreanov and P. A. McClarty, Phys. Rev. B **91**, 064401 (2015).
[15] K. A. Ross, T. Proffen, H. A. Dabkowska, J. A. Quilliam, L. R. Yaraskavitch, J. B. Kycia, and B. D. Gaulin, Phys. Rev. B **86**, 174424 (2012).
[16] A. Yaouanc, P. Dalmas de Réotier, C. Marin, and V. Glazkov, Phys. Rev. B **84**, 172408 (2011).
[17] T. Taniguchi, H. Kadowaki, H. Takatsu, B. Fåk, J. Ollivier, T. Yamazaki, T. J. Sato, H. Yoshizawa, Y. Shimura, T. Sakakibara *et al.*, Phys. Rev. B **87**, 060408 (2013).
[18] K. A. Ross, J. W. Krizan, J. A. Rodriguez-Rivera, R. J. Cava, and C. L. Broholm, Phys. Rev. B **93**, 014433 (2016).
[19] J. W. Krizan and R. J. Cava, Phys. Rev. B **89**, 214401 (2014).
[20] J. W. Krizan and R. J. Cava, J. Phys.: Condens. Matter **27**, 296002 (2015).
[21] J. W. Krizan and R. J. Cava, Phys. Rev. B **92**, 014406 (2015).
[22] M. B. Sanders, J. W. Krizan, K. W. Plumb, T. M. McQueen, and R. J. Cava, J. Phys.: Condens. Matter **29**, 045801 (2016).
[23] M. P. Zinkin, M. J. Harris, and T. Zeiske, Phys. Rev. B **56**, 11786 (1997).
[24] H. Blöte, R. Wielinga, and W. Huiskamp, Physica **43**, 549 (1969).
[25] J. A. Hodges, P. D. de Réotier, A. Yaouanc, P. C. M. Gubbens, P. J. C. King, and C. Baines, J. Phys.: Condens. Matter **23**, 164217 (2011).
[26] W. J. L. Buyers, T. M. Holden, E. C. Svensson, R. A. Cowley, and M. T. Hutchings, J. Phys. C: Solid State Phys. **4**, 2139 (1971).
[27] A. Abragam and B. Bleaney, *Electron Paramagnetic Resonance of Transition Ions* (Oxford University Press, Oxford, 2012).
[28] M. E. Lines, Phys. Rev. **131**, 546 (1963).
[29] J. P. Goff, D. A. Tennant, and S. E. Nagler, Phys. Rev. B **52**, 15992 (1995).
[30] R. M. White, *Quantum Theory of Magnetism*, 3rd ed. (Springer, Berlin, 2006).
[31] K. A. Ross, L. Savary, B. D. Gaulin, and L. Balents, Phys. Rev. X **1**, 021002 (2011).
[32] S. Guitteny, S. Petit, E. Lhotel, J. Robert, P. Bonville, A. Forget, and I. Mirebeau, Phys. Rev. B **88**, 134408 (2013).
[33] H. Yan, O. Benton, L. D. C. Jaubert, and N. Shannon, Phys. Rev. B **95**, 094422 (2017).
[34] J. D. M. Champion and P. C. W. Holdsworth, J. Phys.: Condens. Matter **16**, S665 (2004).
[35] A. Poole, A. S. Wills, and E. Lelievre-Berna, J. Phys.: Condens. Matter **19**, 452201 (2007).
[36] S. Petit, J. Robert, S. Guitteny, P. Bonville, C. Decorse, J. Ollivier, H. Mutka, M. J. P. Gingras, and I. Mirebeau, Phys. Rev. B **90**, 060410 (2014).
[37] J. Gaudet, A. M. Hallas, D. D. Maharaj, C. R. C. Buhariwalla, E. Kermarrec, N. P. Butch, T. J. S. Munsie, H. A. Dabkowska, G. M. Luke, and B. D. Gaulin, Phys. Rev. B **94**, 060407 (2016).
[38] R. Sarkar, J. W. Krizan, F. Brückner, E. C. Andrade, S. Rachel, M. Vojta, R. J. Cava, and H.-H. Klauss, arXiv:1604.00814.
[39] J. P. C. Ruff, J. P. Clancy, A. Bourque, M. A. White, M. Ramazanoglu, J. S. Gardner, Y. Qiu, J. R. D. Copley, M. B.

Johnson, H. A. Dabkowska *et al.*, Phys. Rev. Lett. **101**, 147205 (2008).

[40] J. A. Rodriguez, D. M. Adler, P. C. Brand, C. Broholm, J. C. Cook, C. Brocker, R. Hammond, Z. Huang, P. Hundertmark, J. W. Lynn *et al.*, Meas. Sci. Technol. **19**, 034023 (2008).

[41] G. E. Granroth, D. H. Vandergriff, and S. E. Nagler, Phys. B (Amsterdam, Neth.) **385**, 1104 (2006).

[42] J. Gaudet, D. D. Maharaj, G. Sala, E. Kermarrec, K. A. Ross, H. A. Dabkowska, A. I. Kolesnikov, G. E. Granroth, and B. D. Gaulin, Phys. Rev. B **92**, 134420 (2015).

[43] P. Babkevich, A. Finco, M. Jeong, B. Dalla Piazza, I. Kovacevic, G. Klughertz, K. Krämer, C. Kraemer, D. T. Adroja, E. Goremychkin *et al.*, Phys. Rev. B **92**, 144422 (2015).

[44] K. W. H. Stevens, Proc. Phys. Soc., London, Sect. A **65**, 209 (1952).

[45] M. T. Hutchings, Solid State Phys. **16**, 227 (1964).

[46] M. Rotter, D. Manh Le, J. Keller, L. G. Pascut, T. Hoffmann, M. Doerr, R. Schedler, P. Fabi, S. Rotter, M. Banks, and N. Kluver, McPhase Users Manual: Symmetry Considerations for Crystal Field Parameters, http://www2.cpfs.mpg.de/~rotter/homepage_mcphase/manual/manual.html.

[47] J. Kanamori, Prog. Theor. Phys. **17**, 177 (1957).

[48] G. L. Squires, *Introduction to the Theory of Thermal Neutron Scattering* (Cambridge University Press, Cambridge, UK, 2012).

[49] J. Jensen and A. R. Mackintosh, *Rare Earth Magnetism* (Clarendon Press, Oxford, 1991).

[50] E. A. Oliveira, I. Guedes, A. P. Ayala, J. Y. Gesland, J. Ellena, R. L. Moreira, and M. Grimsditch, J. Solid State Chem. **177**, 2943 (2004).

[51] K. Kimura, S. Nakatsuji, and T. Kimura, Phys. Rev. B **90**, 060414 (2014).

[52] K. Baroudi, B. D. Gaulin, S. H. Lapidus, J. Gaudet, and R. J. Cava, Phys. Rev. B **92**, 024110 (2015).

[53] The $E \sim 360$ meV mode was measured only in NCCF due to time limitations. Given the overall similarity of the other single-ion levels in the two materials, this mode is assumed to lie in same energy range in NSCF.

[54] B. J. Campbell, H. T. Stokes, D. E. Tanner, and D. M. Hatch, J. Appl. Crystallogr. **39**, 607 (2006).

[55] R. D. Shannon, Acta Crystallogr., Sect. A: Cryst. Phys., Diffr., Theor. Gen. Crystallogr. **32**, 751 (1976).

[56] K. Tomiyasu, M. K. Crawford, D. T. Adroja, P. Manuel, A. Tominaga, S. Hara, H. Sato, T. Watanabe, S. I. Ikeda, J. W. Lynn *et al.*, Phys. Rev. B **84**, 054405 (2011).

[57] O. Arnold, J.-C. Bilheux, J. Borreguero, A. Buts, S. I. Campbell, L. Chapon, M. Doucet, N. Draper, R. F. Leal, M. A. Gigg *et al.*, Nucl. Instrum. Methods Phys. Res., Sect. A **764**, 156 (2014).

[58] R. T. Azuah, L. R. Kneller, Y. Qiu, P. L. Tregenna-Piggott, C. M. Brown, J. R. Copley, and R. M. Dimeo, J. Res. Natl. Inst. Stand. Technol. **114**, 341 (2009).

[59] S. W. Lovesey, *Theory of Neutron Scattering from Condensed Matter* (Clarendon Press, Oxford, 1984), Vol. 2.